



A durable P2-type layered oxide cathode with superior low-temperature performance for sodium-ion batteries

Yong Li^{1,2}, Yufeng Zhao^{1,2*}, Xiaochen Feng^{2,3}, Xuan Wang², Qin hao Shi², Jing Wang³, Juan Wang^{1*}, Jiujun Zhang² and Yanglong Hou^{4*}

ABSTRACT To power large-scale energy storage systems, sodium-ion batteries (SIBs) must have not only high-energy density but also high performance under a low-temperature (LT) environment. P2-type manganese oxides with high specific capacity are promising cathode candidates for SIBs, but their LT applications are limitedly explored. We proposed a P2-type $\text{Na}_{0.67}\text{Ni}_{0.1}\text{Co}_{0.1}\text{Mn}_{0.8}\text{O}_2$ material with outstanding LT performance prepared through reasonable structure modulation. The material offers an excellent Na^+ diffusion coefficient (approximately 10^{-9} – $10^{-7.5}$ $\text{cm}^2 \text{s}^{-1}$) at -20°C , a superior LT discharge capacity of $147.4 \text{ mA h g}^{-1}$ in the Na half-cell system, and outstanding LT full cell performance (energy density of $358.3 \text{ W h kg}^{-1}$). Various characterisations and density function theory calculations results show that the solid solution reaction and pseudocapacitive feature promote the diffusion and desolvation of Na^+ from the bulk electrode to interface, finally achieving superior electrochemical performance at LT.

Keywords: sodium-ion batteries, P2-type layered oxides, low temperature, structure modulation, pseudocapacitive feature

INTRODUCTION

Sodium-ion batteries (SIBs) have received considerable attention due to their excellent potential as viable alternatives to lithium-ion batteries (LIBs) in cost-efficient large-scale energy storage systems and low-speed electric vehicles [1,2]. In addition to their cost, safety, and electrochemical performance, low-temperature (LT) properties are vital parameters for their practical applications in the commercial market [3–6]. Thermal management systems are used to ensure that SIBs operate over suitable and favourable temperature range; however, SIBs perform well at LT through not only thermal management but also novel cell design [7,8].

Generally, sodium ions migrate from the electrolyte to the electrode/electrolyte interface and bulk electrode, which corresponds to solvation, desolvation and solid-state diffusion process, respectively. The specific capacities and rate performance can severely deteriorate when the ambient temperature falls to subzero or lower temperature [7,9–17]. LT limitations can be attributed to the reduced conductivity of electrolytes, high barrier for Na^+ desolvation within the electrode/electrolyte inter-

face, and sluggish Na transport kinetics in solid active materials [18–22]. Electrodes with the crystal structure of Na-super-ionic conductors, such as Prussian blue/carbon nanotube composites [23], $\text{Na}_3\text{V}_2(\text{PO}_4)_3/\text{C}$ [24], $\text{Na}_3\text{V}_2(\text{PO}_4)_2\text{O}_2\text{F}$ [25], and $\text{Na}_4\text{Fe}_3(\text{PO}_4)_2(\text{P}_2\text{O}_7)/\text{C}$ [26], are preferred for LT applications. However, their commercial LT application has been hindered due to a lack of rigorous synthesis methods and restricted theoretical capacities. Therefore, the development of high-performance electrode materials that can be charged/discharged at LT is urgent.

We analysed the kinetics, LT electrochemical properties, and storage mechanism of P2- $\text{Na}_{0.67}\text{MnO}_2$ (NM) under LT conditions. Our NM samples offer first LT discharge specific capacity of $108.3 \text{ mA h g}^{-1}$ at 0.2 C ($1 \text{ C} = 170 \text{ mA h g}^{-1}$), which corresponds to a capacity retention of only 52.3% and a poor rate capacity (55 mA h g^{-1} at 10 C). LT cycling stability is merely maintained for <100 cycles at 0.5 C . According to the kinetics analysis, ordered superstructures result in slow desodiation, which further leads to ultrahigh charge transfer resistance. Finally, for Mn sites, partial substitution with Co/Ni having similar ionic radii and different redox potentials (Femi level) can effectively shield the electrostatic interactions of Na^+ /vacancy ordering and enlarge the Na layer distance with transition metal dioxide (TMO_2) slab contraction [27,28]. Thus, an excellent LT and plateau-free P2-type material, $\text{Na}_{0.67}\text{Ni}_{0.1}\text{Co}_{0.1}\text{Mn}_{0.8}\text{O}_2$ (NNCM), was developed. The capacitor behaviour over the entire voltage range ensured both high Na^+ mobility and structural stability at -20°C . NNCM exhibited a high reversible capacity of $147.1 \text{ mA h g}^{-1}$, an excellent rate capacity of 66.8 mA h g^{-1} at 10 C , and an ultrahigh capacity retention of 80% after 300 cycles at -20°C .

EXPERIMENTAL SECTION

Synthesis of NNCM, P2- $\text{Na}_{0.67}\text{Co}_{0.2}\text{Mn}_{0.8}\text{O}_2$ (NCM), P2- $\text{Na}_{0.67}\text{Ni}_{0.2}\text{Mn}_{0.8}\text{O}_2$ (NNM), and NM cathode materials

All the reagents were purchased from Sigma-Aldrich and used without further purification. The NNCM cathode material was prepared using a typical sol–gel method. Citric acid (17 mmol) was dissolved in deionised water (50 mL). Then, different amounts of sodium acetate trihydrate, nickel (II) acetate tetrahydrate, cobalt (II) acetate tetrahydrate, and manganese (II) acetate tetrahydrate, with the total amount of 17 mmol, were

¹ Shaanxi Key Laboratory of Nanomaterials and Nanotechnology, Xi'an University of Architecture and Technology, Xi'an 710055, China

² Institute for Sustainable Energy, College of Science, Shanghai University, Shanghai 200444, China

³ Key Laboratory of Applied Chemistry, Yanshan University, Qinhuangdao 066000, China

⁴ Department of Materials Science and Engineering, College of Engineering, Peking University, Beijing 100871, China

* Corresponding authors (emails: yufengzhao@shu.edu.cn (Zhao Y); juanwang168@gmail.com (Wang J); hou@pku.edu.cn (Hou Y))

mixed according to the desired Na:Ni:Co:Mn ratio. After 30-min stirring, water in the solution was evaporated at 80°C. Subsequently, precursors were dried at 70°C for 24 h. For NNCM, the dried powder was calcined initially at 500°C for 12 h and then at 900°C for another 10 h in air. Finally, after natural cooling, the NNCM samples were obtained. For comparison, the NNM, NCM, and NM samples were synthesised using a similar process. Their chemical formulas were identified using inductively coupled plasma-atomic emission spectrometer (ICP-AES) tests (Table S1).

Characterisation

The crystalline phases of compounds were investigated through powder X-ray diffraction (XRD) on a D8 X-ray diffractometer using Cu K α radiation. The Rietveld refinement of XRD patterns was performed using the FullProf Rietveld program. The morphology and microstructure of the as-prepared materials were analysed through field-emission scanning electron microscopy (FESEM, Nova-450, 15kV) and transmission electron microscopy (TEM, JEOL JEM-2100F TEM, 200kV). Surface chemistry states were determined using X-ray photoelectron spectroscopy (XPS, PHI QUANTERA-II SXM).

Computational details

Density functional theory (DFT) calculations were performed using the Vienna *ab initio* simulation package (VASP) within a $3a \times 4b \times 1c$ supercell. The spin-polarised version of the Perdew–Burke–Ernzerhof functional under the generalised gradient approximation (GGA) was adopted to treat the exchange correlation energy. For the GGA + U -based DFT calculations, the U values of Ni, Co, and Mn were 6.1, 5.7, and 4.0 eV, respectively. All the calculations were performed with an energy cut-off of 400 eV until residual forces in the system became $<0.02 \text{ eV } \text{\AA}^{-1}$ per unit cell. To calculate the energy difference between Na_e and Na_f sites, a $3a \times 4b \times 1c$ supercell with one Na ion was constructed to prevent the Coulombic repulsion among Na ions. The difference in site energy can be calculated using the following equation [25]:

$$\Delta E = E(\text{Na}_e) - E(\text{Na}_f), \quad (1)$$

where $E(\text{Na}_e)$ and $E(\text{Na}_f)$ are the total DFT energies of bulk models with an ion occupying Na_e and Na_f sites, respectively.

Electrochemical measurement

Cathodes were fabricated by blending active materials (80 wt%), super P carbon black (10 wt%), and polyvinylidene fluoride (10 wt%). Then, the slurry obtained was applied onto an aluminium foil, and the foil was dried at 80°C for over 12 h in a vacuum oven. The mass loading of active materials was 1–1.2 mg cm⁻². Half cells were assembled with 2032 type-coin cells in an Ar-containing dry box. The Na metal was used as an anode, and the electrolyte comprised 1 mol L⁻¹ NaPF₆ in a solution of ethylene carbonate and propylene carbonate (1:1 by volume) with 5% fluoroethylene carbonate. Electrochemical tests, including charge/discharge performance analyses and galvanostatic intermittent titration technique (GITT), were conducted using the LAND battery-test instrument (CT2001A). A high-LT chamber (Fig. S1), with a temperature range of –40–60°C, was used to obtain stable ambient temperature for investigations at 25 and –20°C. All the batteries were stored at specific temperature for a minimum of 1 h to attain the equilibrium

between battery and chamber pre-set temperatures. Cyclic voltammetry (CV) and impedance were measured on the Chen Hua electrochemical station (CHI660E) by applying a 5-mV harmonic perturbation signal. Electrochemical impedance spectroscopy (EIS) spectra were acquired in the frequency of 100 kHz to 10 MHz. For GITT measurements, cells were charged in the same voltage window at 0.1 C for 30 min, and then, were relaxed for 2 h. The formula is as follows:

$$D = \frac{4}{\pi\tau} \left(\frac{m_B V_m}{M_B S} \right)^2 \left(\frac{dE_s}{dE_t} \right)^2, \quad (2)$$

where τ is the time for an applied galvanostatic current. M_B and m_B are the molecular weight and mass, respectively, of the active material. V_m is the molar volume, S is the surface area of the electrode, and ΔE_s and ΔE_t are the steady-state (equilibrium) voltage and total change in the cell voltage E during the current pulse, respectively.

RESULTS AND DISCUSSION

Fig. 1a and Figs S2–S5 show the XRD and Rietveld refined results of NM, NCM, NNM, and NNCM, respectively. All the diffraction peaks were assigned to a typical hexagonal structure (space group: $P6_3/mmc$). Table S2 presents the specific crystallographic data, atom coordinates, and occupancies of these compounds. The fitting results and shift of the (002) peak towards a relatively lower angle obtained after the co-substitution of cobalt and nickel indicated that lattice cell expansion along the c -axis and TMO₂ layer contraction led to an increase in the interaction between TM and O and a decrease in the binding energy of Na and O. Finally, ordered superstructures were effectively refrained, because double-ion substitution led to the further enlargement of the Fermi level difference between TMs. At Na_e sites, a preferred occupancy was observed because of low electrostatic repulsion at this position, which can be commonly observed in NNCM compounds. XPS analyses were performed to confirm the oxidation states of Mn, Ni, and Co (Fig. 1b and Fig. S6). The Mn 2p spectra of the two samples were similar, where the binding energy of Mn was between that of trivalent (Mn 2p_{3/2}, 641.2 eV) and tetravalent (Mn 2p_{3/2}, 642.6 eV) Mn states. Moreover, the NNCM sample showed a state considerably similar to the tetravalent state [11,26], and the ratio of Mn⁴⁺ and Mn³⁺ for NNCM was higher than that for the pristine sample. The Mn⁴⁺ contents of the NNCM and pristine samples were 42.1% and 39.6%, respectively. These results indicate that element doping leads to a decrease in high-spin Mn³⁺ formation, which further confirms the stable structure of NNCM compounds. Co/Ni co-doping can expand the Na⁺ layer spacing and accelerate Na⁺ mobility (Fig. 1c). To analyze the visualised microstructure of NM and NNCM powders, the morphology and crystal structure information were acquired through FESEM and TEM, as plotted in Fig. 1d and Fig. S7. The NNCM particles exhibited a microflake structure, which highly promoted the electrode–electrolyte contact and shortened the diffusion distance. The widths of approximately 2.5 and 5.5 Å between the neighbouring lattice fringes determined using high-resolution TEM (HRTEM) corresponded to the d -spacing values of the (100) and (002) planes, respectively, of the layered hexagonal structure of NNCM particles (Fig. 1e–g). The selected area electron diffraction (SAED) further confirmed that TM atoms were arranged in the typical hexagonal symmetry phase [27]. Moreover, energy-dispersive spectroscopy (EDS) mapping

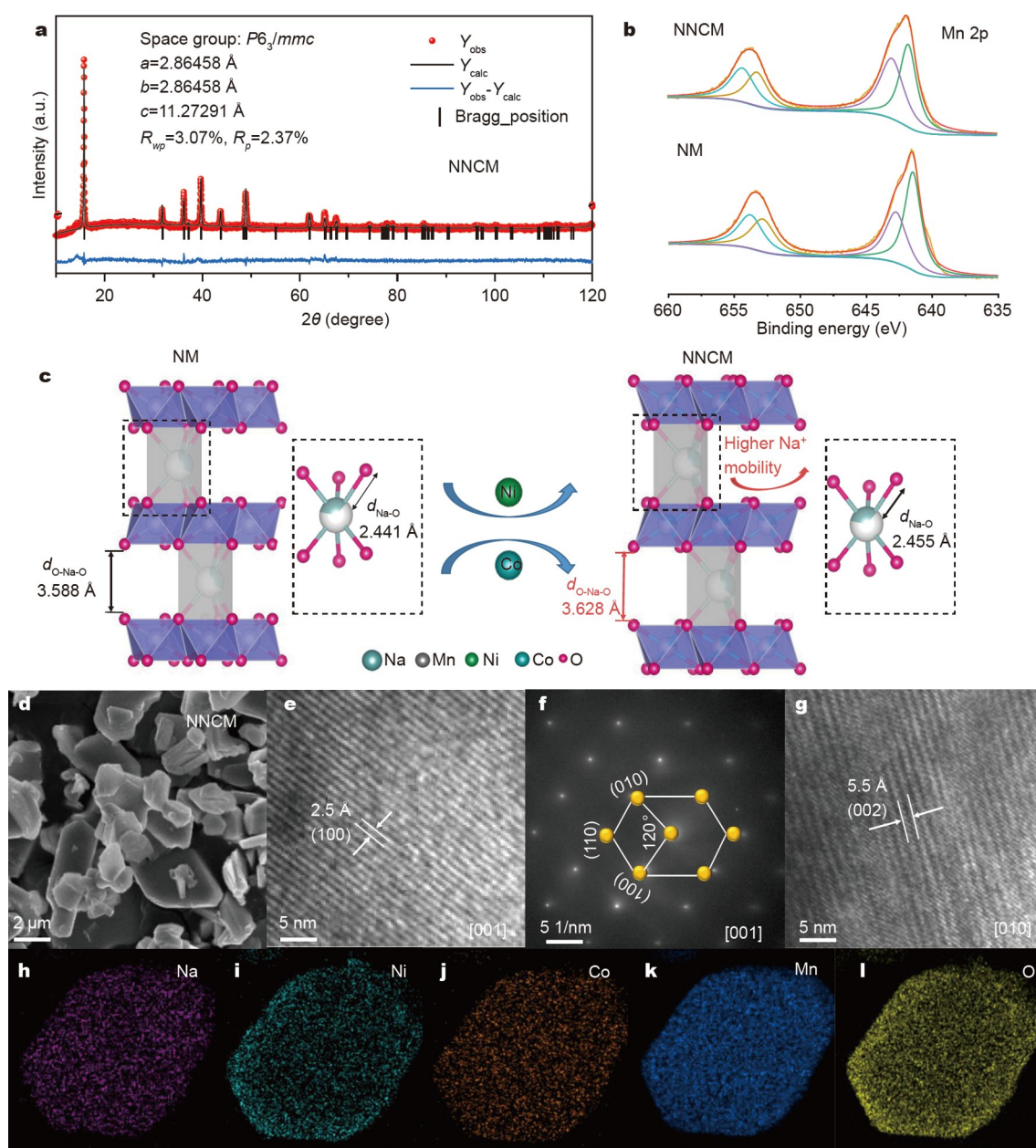


Figure 1 Structural characterisation of NM and NNCM. (a) Rietveld refinement results of the NNCM powder, (b) Mn 2p XPS fitted spectra of NM and NNCM powders, (c) schematic illustration of the effect of Ni and Co doping on the electrode structure, (d) SEM, (e and f) HRTEM image at the [001] zone axis and the corresponding SAED image, (g) HRTEM image at the [010] zone axis, and (h–l) TEM (HAADF Na, Ni, Co, Mn, and O) elemental mapping images of the NNCM powder.

shows a uniform element distribution of Na, Ni, Co, Mn, and O in the NNCM cathode material (Fig. 1h–l).

The Na-storage electrochemical properties of NNCM and NM compounds were systematically cycled as the cathode in half cells at 25 and -20°C . Fig. 2a presents the room-temperature (RT) galvanostatic charge/discharge profiles and the corresponding dQ/dV plots upon cycling. In 1.5–4.2 V at 0.2 C, the NNCM samples provided a discharge-specific capacity of 181.5 mA h g^{-1} , which is $<207.1\text{ mA h g}^{-1}$ for NM. The charge-discharge curves and the corresponding dQ/dV plots of the NM samples exhibiting complex voltage plateaus and steps transformed into relatively highly smoother charge-discharge curves after substitution and cycling, and in particular, the clear sloping

line observed over 2 V. Similarly, the voltage plateaus of the NM samples remained complex when the ambient temperature decreased to -20°C (Fig. 2b) (denoted as NM-LT and NNCM-LT). The curve corresponding to NNCM-LT is a complete sloping line. Moreover, NNCM-LT exhibited an ultrahigh LT-specific capacity (147.4 mA h g^{-1}), thereby outperforming NM-LT electrodes (108.3 mA h g^{-1}). These high performance results indicate the transformation of the electrochemical behaviour to capacitor behaviour, effective suppression of Na^+ /vacancy ordered rearrangement, and phase transition. The compounds with a single element (Co or Ni) occupied in Mn sites maintained the Na^+ /vacancy ordered behaviour (Fig. S8). These findings again confirm that TM ions (Mn^{3+} , Ni^{2+} , and Co^{3+}) with

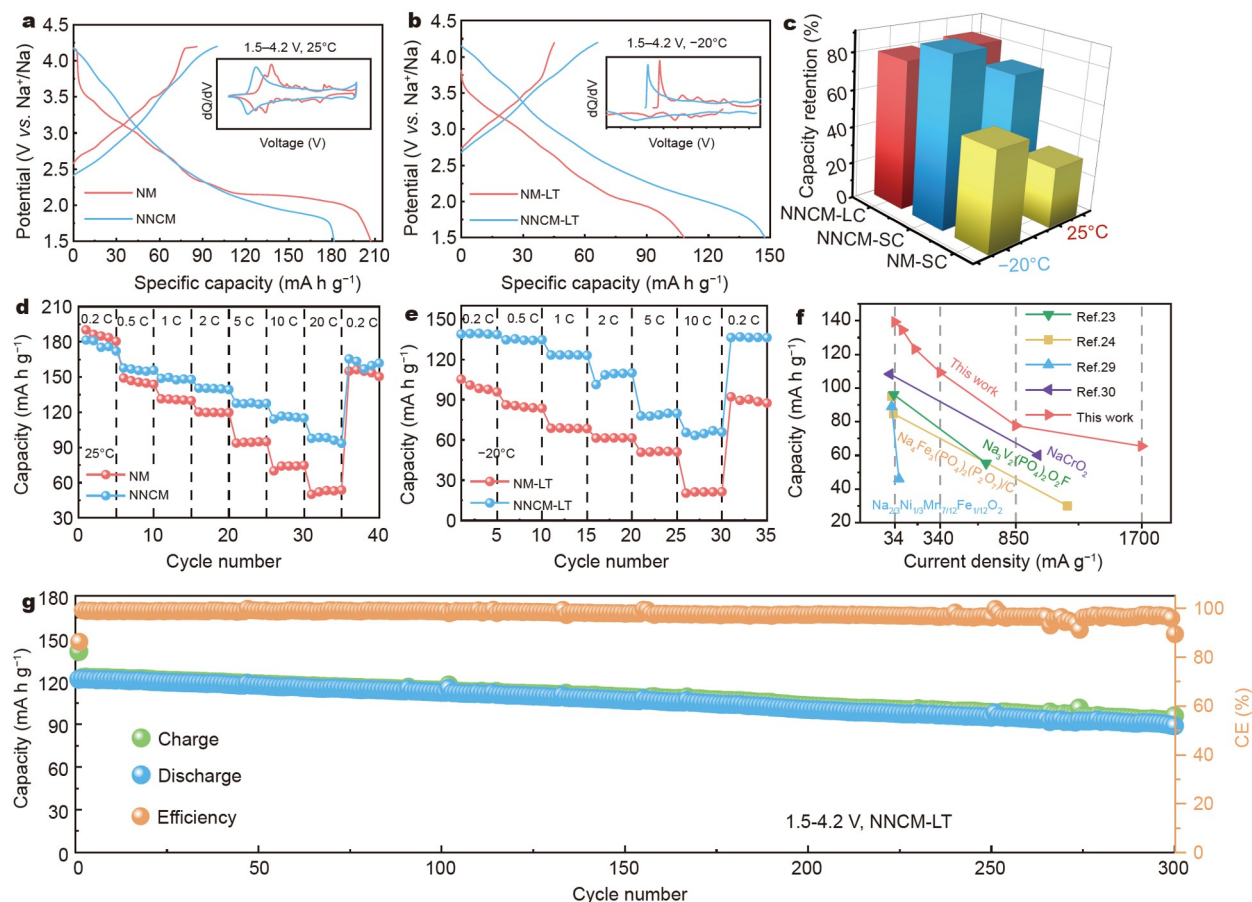


Figure 2 Electrochemical characterisations of the NM and NNCM electrodes in Na half cells at 25 and -20°C . (a and b) Galvanostatic charge/discharge curves and dQ/dV profiles (inset) at 0.2 C. (c) Capacity retentions corresponding to various cycles (SC: 100 cycles; LC: 300 cycles). (d and e) Rate capabilities at different rates. (f) Rate performance compared with some advanced electrodes at LT. (g) Long-term cycle performance of NNCM-LT at 1 C.

highly similar ionic radii ($\text{Co}^{3+} = 6.1 \text{ \AA}$, $\text{Ni}^{2+} = 6.9 \text{ \AA}$, and $\text{Mn}^{3+} = 6.5 \text{ \AA}$) and substantially different redox potentials ($\sim 3 \text{ V}$ for $\text{Co}^{3+/4+}$, $\sim 3.3/3.7 \text{ V}$ for $\text{Ni}^{2+/3+/4+}$, and $\sim 2.3 \text{ V}$ for $\text{Mn}^{3+/4+}$) build the P2-layered oxide-free Na^+ /vacancy ordering, which can extend the complete solid solution zone over a wide Na intercalation range, thus ensuring rapid Na^+ mobility [25,27,28]. Fig. S9 presents their corresponding CV curves. The CV of NM shows a sharp peak after 4 V, corresponding to the unfavourable phase transition from P2 to O2 at 25°C . Additionally, the distinct polarisation voltage (805 mV) for NM-LT indicated an unstable structure at -20°C . The NNCM samples resembled capacitors and exhibited low polarisation voltage (485 mV). After 100 cycles at 0.5 C (Fig. S10a and S10b), NNCM exhibited excellent capacity retention (NNCM: 74%; NNCM-LT: 91%). By contrast, the NM samples showed the capacity retention of only 32.2% at 25°C . Although the NM electrode performed well during 90 cycles, the LT cell broke after the 98th cycle. The charge–discharge curves showed distinct overcharge caused by the complicated LT effect (slow kinetics and solvation/desolvation processes), which led to the disruption of sodium cathode material stability (Fig. S10c). The LT effect caused a decrease in the ionic conductivity and an increase in the transfer resistance, thus leading to the difficult Na-intercalation/extraction and irreversible gliding of oxygen layers. Then, the lattice mismatch and dislocations formed, which ultimately marred the electrochemical performance. By contrast, the NNCM-LT material,

which exhibited sloping lines without discharge voltage plateaus, showed a typical solid-solution reaction, where variations in the volume and lattice parameters were negligible, and excellent kinetics after cycling (Fig. S10d). The NNCM compounds showed an outstanding capacity retention of 82.3% after 200 cycles at 2 C and 1.5–4.2 V and a stable Coulombic efficiency (Fig. S11). The LT-capacity retention for NNCM reached 80% after 300 cycles at 1 C (Fig. 2g). Fig. 2c illustrates the detailed capacity retentions at various cycles (LC: long cycle; SC: short cycle). To further investigate rate properties, the NM and NNCM electrodes were compared at various rates (Fig. 2d). NNCM provided the reversible discharge capacities of 180.9, 156.8, 148.8, 140.2, 127.6, 116.2, and 98.4 mA h g^{-1} at 0.2, 0.5, 1, 2, 5, 10, and 20 C, respectively. By contrast, NM offered the reversible capacities of only 74.2 and 53 mA h g^{-1} at 10 and 20 C, respectively. NNCM-LT exhibited an excellent LT rate (Fig. 2e), with the discharge capacities of 123.2, 79.8, and 66.8 mA h g^{-1} at 1, 5, and 10 C, respectively, which surpassed those capacities of NM-LT and some previously reported sodium cathode materials [23,24,29,30].

To further understand the reason for excellent electrochemical performance, especially for outstanding LT properties, we investigated the NNCM electrode kinetics irrespective of RT or LTs. The CV of NNCM and NNCM-LT was measured at various scan rates (Fig. 3a and d). With an increase in the scan rate, the cathodic and anodic peaks shifted to relatively low and high

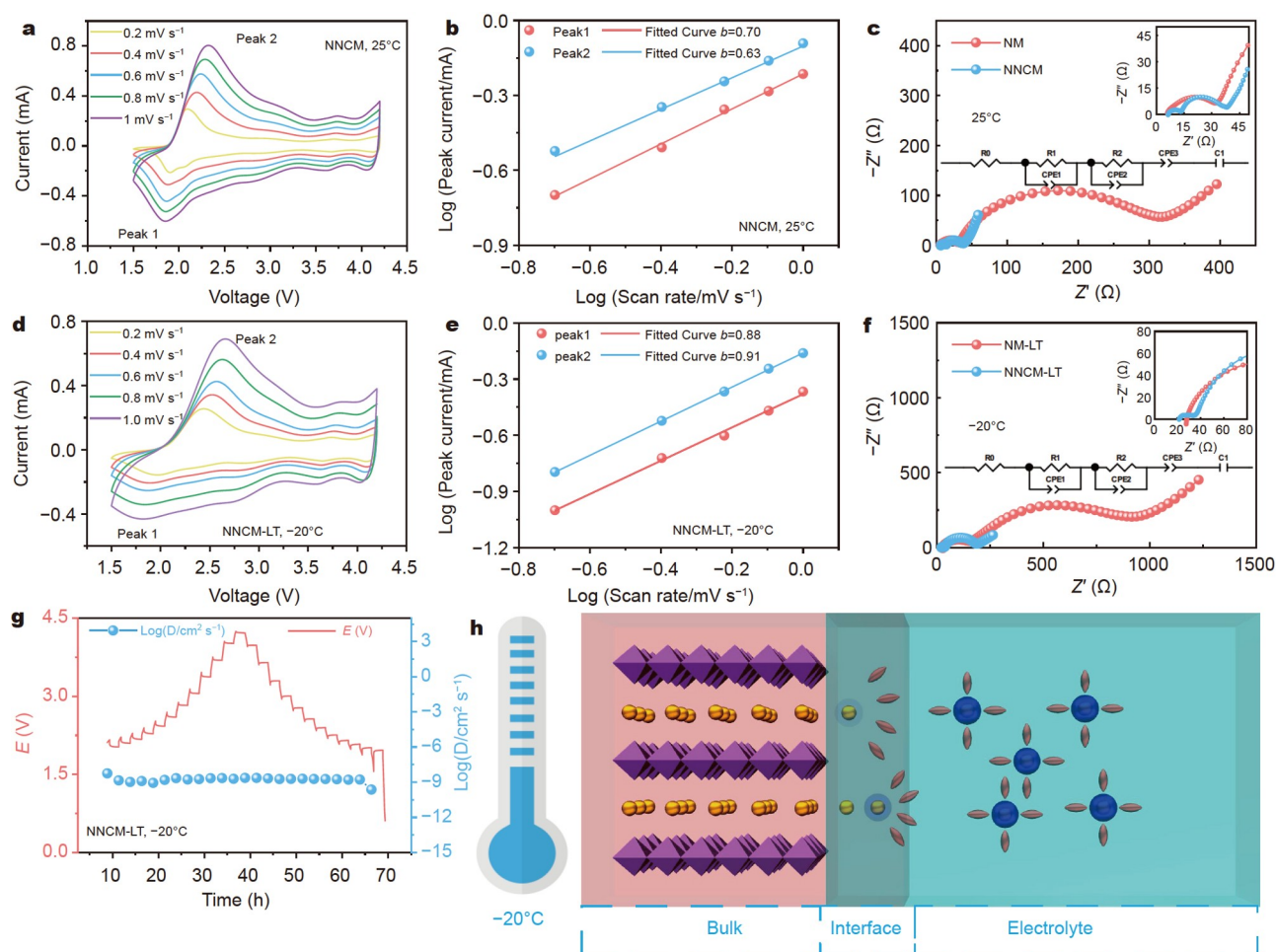


Figure 3 Kinetics analyses of sodium storage for the NNCM electrode at 25 and -20°C . CV of (a) NNCM and (d) NNCM-LT electrode responses with various scan rates of $0.2\text{--}1\text{ mV s}^{-1}$. Determination of the b value for (b) NNCM and (e) NNCM-LT electrodes according to the $\log(v)\text{--}\log(i)$ relationship. EIS curves of (c) NNCM and (f) NNCM-LT electrodes. GITT curves of (g) NNCM-LT electrodes. (h) Sodiation with the synergistic effect of the surface-controlled intercalation pseudocapacitive behaviour at the interface and high diffusion coefficient in the bulk electrode.

potential ranges, respectively, indicating the presence of combined diffusion-controlled and capacitive behaviours. In theory, the scan rate (v) and the measured current (i) comply with Equations (3–6) proposed by Dunn's group [31,32]:

$$i = av^b, \quad (3)$$

$$\log(i) = b\log(v) + \log(a), \quad (4)$$

where a and b are the empirical parameters, and i is the peak current. The b value can be determined by plotting a $\log(i)\text{--}\log(v)$ graph. The b value of 0.5 indicates a diffusion-controlled process, and when the b value approaches 1, the capacitive process (surface-driven behaviour) becomes dominant. We calculated the b value at the oxidation peaks of 2.12 and 2.25 V and at the reduction peak of 1.78 V (Fig. 3b and e). The b values of both the NNCM and NNCM-LT electrodes are >0.5 , indicating that the kinetics are primarily surface-controlled intercalation pseudocapacitive behaviour, and thus, are fast.

$$i = k_1v^{1/2} + k_2v, \quad (5)$$

$$i/v^{1/2} = k_1 + k_2v^{1/2}, \quad (6)$$

where k_1 and k_2 are constants, k_2v and $k_1v^{1/2}$ represent the contribution rates of capacitance and Faradaic intercalation in

the electrochemical reaction, respectively. The NNCM and NNCM-LT electrodes exhibited high capacitive behaviour ratios at all the rates (Fig. S12). Such features can help overcome the problem of slow solid-diffusion in the electrolyte/electrode interface, which is often considered an impeding factor for SIB operations at LT [16]. EIS was used to evaluate the transport kinetics (Fig. 3c and f). According to the combined EIS and Z view software analyses, one branch, representing the first semi-circle at mid frequencies, showed the desolvation behaviour at the interface. The second semi-circle at mid frequencies exhibited the charge transfer phenomenon occurring at the electrode. The second branch comprised a diffusion element at low frequencies [33]. Therefore, the resistive contribution described using the equivalent circuit model can be divided into three major categories: high-frequency Ohmic resistance (R_0), solid electrolyte interphase resistance (R_1), and charge transfer resistance (R_2). Table S3 presents all the resistances of NNCM calculated from the EIS data. The optimised ionic and electronic pathways were obtained for the modified compounds with disordered structures (Table S3). When the cycling temperature decreased to -20°C , the small variation in R_1 values and low charge-transfer resistance of the NNCM electrode provided stable desolvation and relatively higher electro-activities at the

interface, which indicated a high LT rate capacity and cycling stability [34]. To further probe the Na^+ diffusion coefficient (D_{Na^+}) of NNCM-LT and other samples, GITT was conducted (Fig. 3g and Fig. S13). The D_{Na^+} value determined from GITT for NNCM was approximately 10^{-9} – $10^{-7.5}$ $\text{cm}^2 \text{s}^{-1}$, which is three orders of magnitude higher than D_{Na^+} for NM ($10^{-12.5}$ – $10^{-10.5}$ $\text{cm}^2 \text{s}^{-1}$) at 25°C. When the temperature decreased to -20°C , D_{Na^+} for NNCM-LT remained within 10^{-9} – $10^{-7.5}$ $\text{cm}^2 \text{s}^{-1}$, and that for NM-LT ($10^{-13.5}$ – 10^{-11} $\text{cm}^2 \text{s}^{-1}$) decreased to an order of magnitude lower than that for NM. Moreover, no jumps were observed in Na diffusion coefficient values for NNCM-LT, which can be attributed to Na-vacancy disorder in the bulk and is consistent with the sloping characteristic of electrochemical curves. Fig. 3h illustrates the sodiation of the NNCM electrode. Na-vacancy disorder led to the solid solution reaction in the bulk electrode, and the pseudocapacitive feature promoted Na^+ desolvation at the electrolyte/electrode interface, thus achieving high electrochemical performance at LT.

To further obtain insights into the structural evolution of the NNCM samples during desodiation/sodiation, *in situ* XRD was employed at 0.2 C and 1.5–4.2 V during the initial cycle (Fig. 4a). Fig. 4b illustrates the corresponding lattice constants (*a* and *c*). When sodium ions were extracted, no new peaks appeared, but the (002) and (004) peaks of NNCM consecutively shifted towards a relatively low angle. By contrast, the (100) and (102) diffraction lines shifted towards a relatively high angle. During discharge, the shifted diffraction peaks regained their original position, which confirmed the structural robustness of NNCM after cycling. The (004) diffraction lines did not appear in any peak split or shape change, which indicated the absolute solid-solution behaviour of NNCM [27]. The volume change of unit cells obtained before and after Na^+ extraction was only 1.4%, which accounted for the durable electrochemical performance

[35]. Therefore, double atoms (Co and Ni) diminished phase transformation after cycling. Such a solid-solution behaviour provides excellent kinetic transportation.

From DFT, we calculated the projected density of states (pDOS) for 3d orbitals of TMs and 2p orbitals of oxygen. In theory, TM and O atoms have octahedral coordination (TMO_6 octahedral structure) in layered TM oxides, and the energy levels of 3d orbitals of the central TM ions split into two orbitals, a high-energy e_g orbital and low-energy t_{2g} orbital [36]. Mn ions show distinct energy levels for different samples (Fig. 5a). In NNCM, Mn ions exhibit a high oxidation state (Mn^{4+} : $t_{2g}^3 e_g^0$), and in the NM, they show Mn^{3+} : $t_{2g}^3 e_g^1$. Mn^{3+} with unpaired electrons exhibits a strong Jahn–Teller activity, which leads to orbital, spin, and charge ordering, thereby restricting desodiation/sodiation [37]. Furthermore, the calculated total DFT energy shows that Ni/Co/Mn mixing results in a considerable decrease in the site energy difference from Na_e to Na_b , and thus, promotes the occurrence of Na^+ /vacancy order–disorder [25] (Fig. 5b and c).

Finally, to investigate its application in LT full cells, the NNCM cathode was coupled with a hard carbon (HC) anode (the mass ratio of 1.2:1) (Fig. 6a). Before assembling the full battery, the solid-electrolyte formation must be facilitated through presodiation for the HC anode. The full battery at RT exhibits a high reversible specific capacity of 178.5 mA h g^{-1} with a specific energy of 449 Wh kg^{-1} at 0.2 C in 1.4–4.1 V based on the cathode mass (Fig. 6b). The full battery shows a reversible specific capacity of 142.4 mA h g^{-1} at -20°C , corresponding to an energy density of 358.3 Wh kg^{-1} , which is 79.8% of its RT capacity. Fig. 6c and d illustrate the rate properties. At 0.2, 0.5, 1, 2, 5, and 10 C, the RT full cell can offer the reversible capacities of 178.5, 158.7, 148.4, 134.9, 114.9, and 92 mA h g^{-1} , respectively, and its LT rate capacities are 79.8%, 77%, 67%, 53.7%, 61.9%,

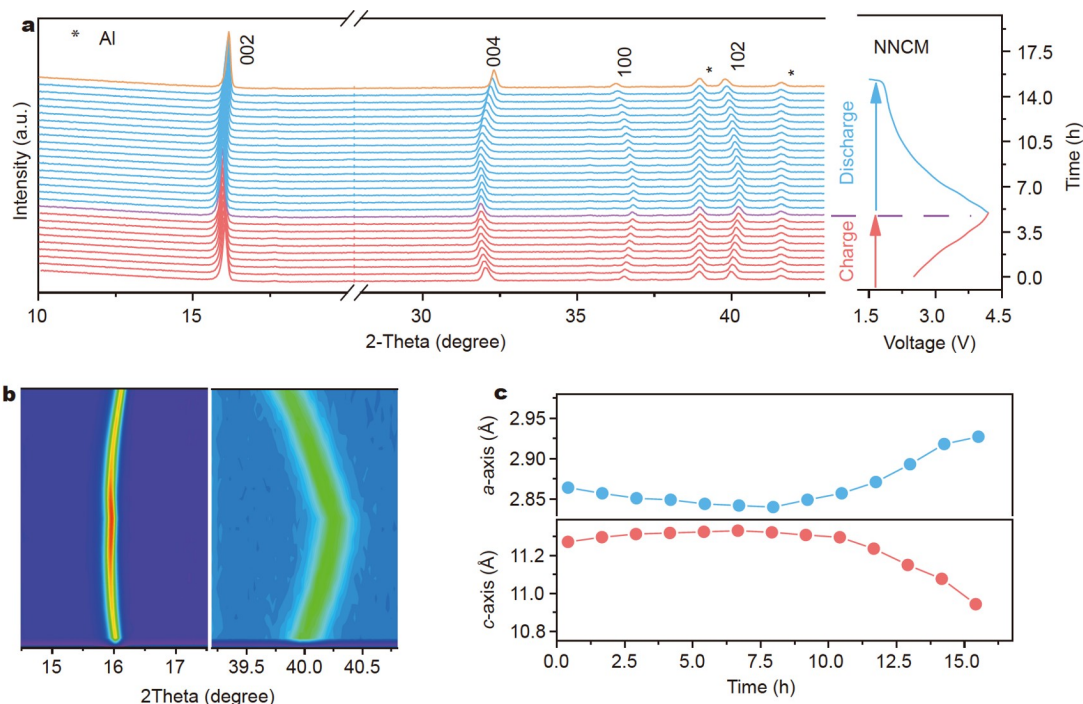


Figure 4 Crystal structural evolution of NNCM after Na^+ extraction/insertion. (a) *In situ* XRD patterns collected during the first charge/discharge cycle of the NNCM electrode at 0.2 C and 1.5–4.2 V. (b) The corresponding contour map for the evolution of the main characteristic diffraction peaks. (c) Variation in the lattice constant along with Na^+ extraction and insertion for NNCM.

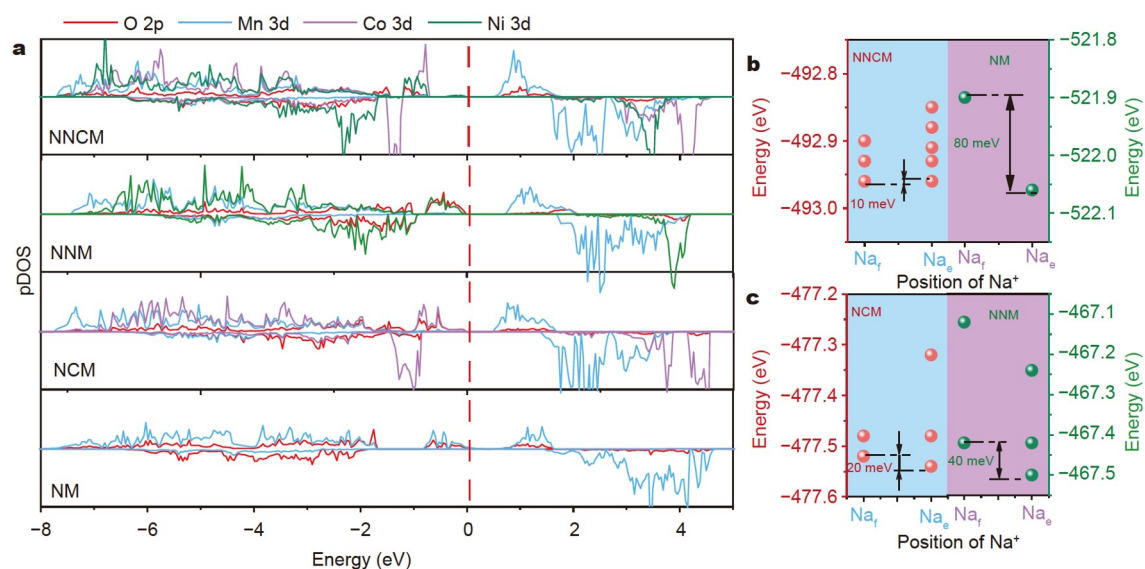


Figure 5 (a) Projected density of states of NM, NCM, NNM and NNCM. (b and c) Calculated energy difference between Na_e and Na_f sites for NM, NCM, NNM, and NNCM.

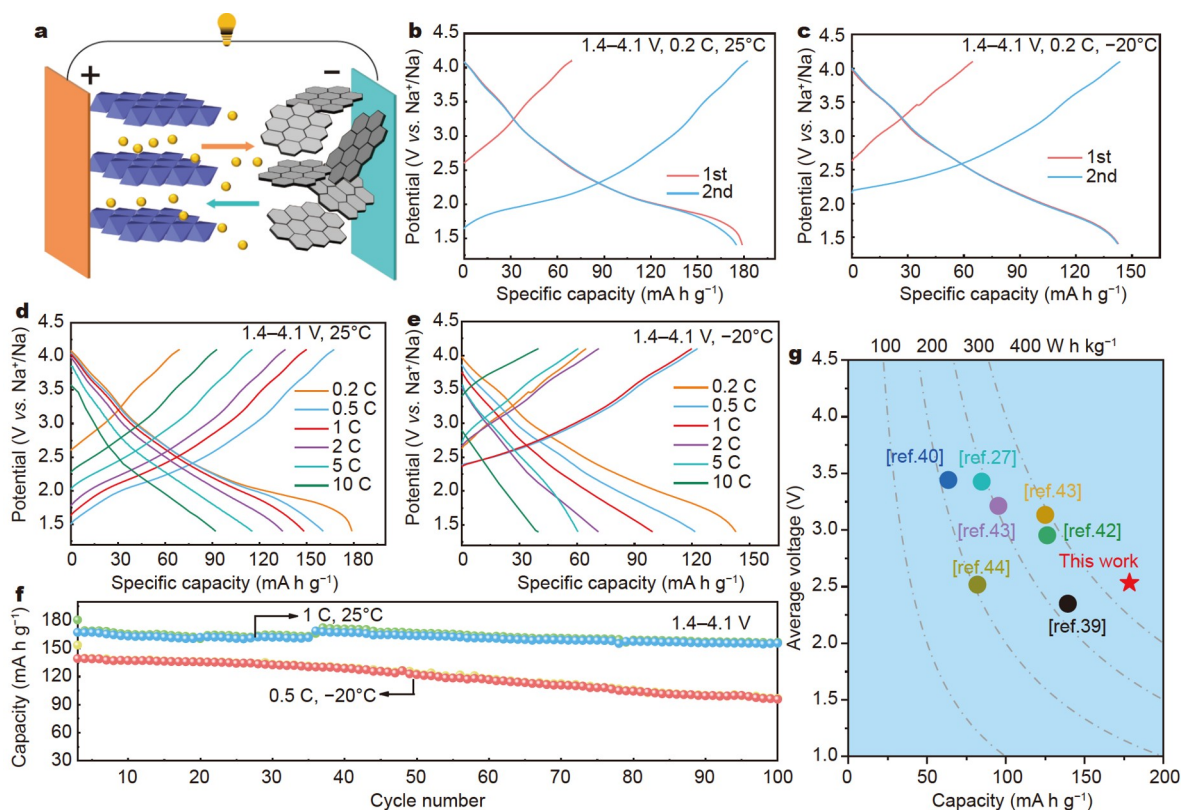


Figure 6 Full cell performance of the NNCM electrode at 25 and -20°C . (a) Na-ion full cell coupled with NNCM as the cathode and HC as the anode. (b and c) Charge/discharge curves of the full cell in 1.4–4.1 V at 0.2 C. (d and e) Various rate curves of NNCM//HC. (f) Cycle performance of the full cell at 0.5 and 1 C during 100 cycles. (g) Full cell performance of NNCM and other available Na-ion battery systems based on the cathode mass. All the reported data are converted into the capacity by using the same method.

and 43.5% of its RT capacities, respectively, which further confirms its superior rate capacity. Our NNCM electrode with enhanced Na⁺ diffusivity exhibits an excellent long-term cycle, and its capacity retention is 93% at 1 C and 25°C and 68.2% at 0.5 C and -20°C (Fig. 6f). Our NNCM//HC full cell is outstanding and comparable to most previously reported full cells

(Fig. 6g) [38–44]. These results indicate that the NNCM electrode is feasible and prospective for high-energy-storage systems.

CONCLUSIONS

We studied the LT electrochemical properties and storage

mechanism of P2-type Mn-based layered cathode oxides through various cycling measurements and kinetic analyses. In the crystal framework, LT electrochemical performance was highly hindered due to Na⁺/vacancy order, which induced slow LT Na⁺ mobility and solvation/desolvation, leading to high transfer resistances, difficult Na-intercalation/extraction, and irreversible gliding of oxygen layers. Eventually, lattice mismatch and dislocations occurred. Therefore, we designed the LT P2-type layered cathode material through optimal structure modulation with the partial element substitution of Ni and Co into Mn sites. DFT calculations demonstrated that the double atoms (Co and Ni) highly inhibited the Jahn–Teller activity of Mn ions, minimised the site energy difference between Na_e and Na_f, and increased the difference in Fermi levels between TMs, thereby increasing the degree of Na-vacancy disorders and enlarging interstitial spaces. With its open ionic channels and enlarged Na interlayers, NNCM exhibits high Na⁺ diffusion coefficients (approximately 10^{−8} cm² s^{−1} at 25°C and 10^{−9} cm² s^{−1} at −20°C) and intercalation pseudocapacitive behaviour, which provides excellent LT electrochemical properties for SIBs. Consequently, unique electrodes offer brilliant LT electrochemical properties. Our findings shed light on the applications of energy-storage systems and make progress towards SIB commercialisation.

Received 21 April 2021; accepted 17 June 2021;
published online 4 August 2021

- Hwang JY, Myung ST, Sun YK. Sodium-ion batteries: present and future. *Chem Soc Rev*, 2017, 46: 3529–3614
- Wang X, Roy S, Shi Q, *et al.* Progress in and application prospects of advanced and cost-effective iron (Fe)-based cathode materials for sodium-ion batteries. *J Mater Chem A*, 2021, 9: 1938–1969
- Wang C, Du D, Song M, *et al.* A high-power Na₃V₂(PO₄)₃-Bi sodium-ion full battery in a wide temperature range. *Adv Energy Mater*, 2019, 9: 1900022
- Wang YY, Hou BH, Guo JZ, *et al.* An ultralong lifespan and low-temperature workable sodium-ion full battery for stationary energy storage. *Adv Energy Mater*, 2018, 8: 1703252
- Hou BH, Wang YY, Liu DS, *et al.* N-doped carbon-coated Ni_{1.8}Co_{1.2}Se₄ nanoaggregates encapsulated in N-doped carbon nanoboxes as advanced anode with outstanding high-rate and low-temperature performance for sodium-ion half/full batteries. *Adv Funct Mater*, 2018, 28: 1805444
- Zhao N, Zhang F, Zhan F, *et al.* Fe³⁺-stabilized Ti₃C₂T_x MXene enables ultrastable Li-ion storage at low temperature. *J Mater Sci Tech*, 2021, 67: 156–164
- Hou J, Yang M, Wang D, *et al.* Fundamentals and challenges of lithium ion batteries at temperatures between −40 and 60 °C. *Adv Energy Mater*, 2020, 10: 1904152
- Gupta A, Manthiram A. Designing advanced lithium-based batteries for low-temperature conditions. *Adv Energy Mater*, 2020, 10: 2001972
- Nian Q, Wang J, Liu S, *et al.* Aqueous batteries operated at −50 °C. *Angew Chem Int Ed*, 2019, 58: 16994–16999
- Hwang JY, Oh SM, Myung ST, *et al.* Radially aligned hierarchical columnar structure as a cathode material for high energy density sodium-ion batteries. *Nat Commun*, 2015, 6: 6865
- Li Y, Shi Q, Yin X, *et al.* Construction nasicon-type NaTi₂(PO₄)₃ nanoshell on the surface of P2-type Na_{0.67}Co_{0.2}Mn_{0.8}O₂ cathode for superior room/low-temperature sodium storage. *Chem Eng J*, 2020, 402: 126181
- Yin X, Sarkar S, Shi S, *et al.* Recent progress in advanced organic electrode materials for sodium-ion batteries: Synthesis, mechanisms, challenges and perspectives. *Adv Funct Mater*, 2020, 30: 1908445
- Shen L, Li Y, Roy S, *et al.* A robust carbon coating of Na₃V₂(PO₄)₃ cathode material for high performance sodium-ion batteries. *Chin Chem Lett*, 2021, doi: 10.1016/j.ccllet.2021.03.005
- Dong X, Lin Y, Li P, *et al.* High-energy rechargeable metallic lithium battery at −70 °C enabled by a cosolvent electrolyte. *Angew Chem Int Ed*, 2019, 58: 5623–5627
- Shen L, Shi S, Roy S, *et al.* Recent advances and optimization strategies on the electrolytes for hard carbon and P-based sodium-ion batteries. *Adv Funct Mater*, 2020, 31: 2006066
- Jin Y, Xu Y, Le PML, *et al.* Highly reversible sodium ion batteries enabled by stable electrolyte-electrode interphases. *ACS Energy Lett*, 2020, 5: 3212–3220
- Yue R, Xia F, Qi R, *et al.* Trace Nb-doped Na_{0.7}Ni_{0.3}Co_{0.1}Mn_{0.6}O₂ with suppressed voltage decay and enhanced low temperature performance. *Chin Chem Lett*, 2021, 32: 849–853
- Tie D, Gao G, Xia F, *et al.* Modulating the interlayer spacing and Na⁺/vacancy disordering of P2-Na_{0.67}MnO₂ for fast diffusion and high-rate sodium storage. *ACS Appl Mater Interfaces*, 2019, 11: 6978–6985
- Dong X, Yang Y, Wang B, *et al.* Low-temperature charge/discharge of rechargeable battery realized by intercalation pseudocapacitive behavior. *Adv Sci*, 2020, 7: 2000196
- Gao G, Tie D, Ma H, *et al.* Interface-rich mixed P2 + T phase Na_xCo_{0.1}Mn_{0.9}O₂ (0.44 ≤ x ≤ 0.7) toward fast and high capacity sodium storage. *J Mater Chem A*, 2018, 6: 6675–6684
- You Y, Yao HR, Xin S, *et al.* Subzero-temperature cathode for a sodium-ion battery. *Adv Mater*, 2016, 28: 7243–7248
- Rui X, Zhang X, Xu S, *et al.* A low-temperature sodium-ion full battery: Superb kinetics and cycling stability. *Adv Funct Mater*, 2020, 31: 2009458
- Guo JZ, Wang PF, Wu XL, *et al.* High-energy/power and low-temperature cathode for sodium-ion batteries: *In situ* XRD study and superior full-cell performance. *Adv Mater*, 2017, 29: 1701968
- Chen M, Hua W, Xiao J, *et al.* NASICON-type air-stable and all-climate cathode for sodium-ion batteries with low cost and high-power density. *Nat Commun*, 2019, 10: 1480
- Wang PF, Yao HR, Liu XY, *et al.* Na⁺/vacancy disordering promises high-rate Na-ion batteries. *Sci Adv*, 2018, 4: eaar6018
- Hwang J, Kim J, Yu T, *et al.* A new P2-type layered oxide cathode with extremely high energy density for sodium-ion batteries. *Adv Energy Mater*, 2019, 9: 1803346
- Xiao Y, Zhu Y, Yao H, *et al.* A stable layered oxide cathode material for high-performance sodium-ion battery. *Adv Energy Mater*, 2019, 9: 1803978
- Wang Y, Xiao R, Hu YS, *et al.* P2-Na_{0.6}[Cr_{0.6}Ti_{0.4}]O₂ cation-disordered electrode for high-rate symmetric rechargeable sodium-ion batteries. *Nat Commun*, 2015, 6: 6954
- Yang Q, Wang PF, Guo JZ, *et al.* Advanced P2-Na_{2/3}Ni_{1/3}Mn_{7/12}Fe_{1/12}O₂ cathode material with suppressed P2–O₂ phase transition toward high-performance sodium-ion battery. *ACS Appl Mater Interfaces*, 2018, 10: 34272–34282
- Liang L, Sun X, Denis DK, *et al.* Ultralong layered NaCrO₂ nanowires: A competitive wide-temperature-operating cathode for extraordinary high-rate sodium-ion batteries. *ACS Appl Mater Interfaces*, 2019, 11: 4037–4046
- Augustyn V, Come J, Lowe MA, *et al.* High-rate electrochemical energy storage through Li⁺ intercalation pseudocapacitance. *Nat Mater*, 2013, 12: 518–522
- Choi C, Ashby DS, Butts DM, *et al.* Achieving high energy density and high power density with pseudocapacitive materials. *Nat Rev Mater*, 2019, 5: 5–19
- Laforge A, Yuan XZ, Platt A, *et al.* Effects of fast charging at low temperature on a high energy Li-ion battery. *J Electrochem Soc*, 2020, 167: 140521
- Liao B, Li H, Xu M, *et al.* Designing low impedance interface films simultaneously on anode and cathode for high energy batteries. *Adv Energy Mater*, 2018, 8: 1800802
- Jin T, Wang PF, Wang QC, *et al.* Realizing complete solid-solution reaction in high sodium content P2-type cathode for high-performance sodium-ion batteries. *Angew Chem Int Ed*, 2020, 59: 14511–14516
- Sun G, Yu FD, Que LF, *et al.* Local electronic structure modulation

- enhances operating voltage in Li-rich cathodes. *Nano Energy*, 2019, 66: 104102
- 37 Radin MD, Van der Ven A. Simulating charge, spin, and orbital ordering: Application to Jahn–Teller distortions in layered transition-metal oxides. *Chem Mater*, 2018, 30: 607–618
 - 38 Li X, Ma X, Su D, *et al.* Direct visualization of the Jahn–Teller effect coupled to Na ordering in $\text{Na}_{0.8}\text{MnO}_2$. *Nat Mater*, 2014, 13: 586–592
 - 39 Zhu YF, Xiao Y, Hua WB, *et al.* Manipulating layered P2@P3 integrated spinel structure evolution for high-performance sodium-ion batteries. *Angew Chem Int Ed*, 2020, 59: 9299–9304
 - 40 Wang QC, Meng JK, Yue XY, *et al.* Tuning P2-structured cathode material by Na-site Mg substitution for Na-ion batteries. *J Am Chem Soc*, 2019, 141: 840–848
 - 41 Xiao Y, Wang PF, Yin YX, *et al.* Exposing {010} active facets by multiple-layer oriented stacking nanosheets for high-performance capacitive sodium-ion oxide cathode. *Adv Mater*, 2018, 30: 1803765
 - 42 Ye H, Wang CY, Zuo TT, *et al.* Realizing a highly stable sodium battery with dendrite-free sodium metal composite anodes and O3-type cathodes. *Nano Energy*, 2018, 48: 369–376
 - 43 Zhou K, Xie Q, Li B, *et al.* An in-depth understanding of the effect of aluminum doping in high-nickel cathodes for lithium-ion batteries. *Energy Storage Mater*, 2021, 34: 229–240
 - 44 Mu L, Xu S, Li Y, *et al.* Prototype sodium-ion batteries using an air-stable and Co/Ni-free O3-layered metal oxide cathode. *Adv Mater*, 2015, 27: 6928–6933

Acknowledgements We thank the financial support from the National Natural Science Foundation of China (51774251), Shanghai Science and Technology Commission’s “2020 Science and Technology Innovation Action Plan” (20511104003), the Natural Science Foundation of Shanghai (21ZR1424200), Hebei Natural Science Foundation for Distinguished Young Scholars (B2017203313), and Talent Engineering Training Funds of Hebei Province (A201802001).

Author contributions Zhao Y, Wang J, Hou Y and Zhang J designed and guided the work. Li Y performed the experiments. Feng X and Wang J performed the first-principles calculations. Li Y wrote the paper with support from Wang X and Shi Q. All authors contributed to the general discussion.

Conflict of interest The authors declare no conflict of interest.

Supplementary information Supporting data are available in the online version of the paper.



Yong Li is a PhD student of Xi'an University of Architecture and Technology under the supervision of Prof. Juan Wang. Currently, he is studying at Shanghai University as an exchange student in Prof. Yufeng Zhao's group. His research is mainly focused on the low-temperature sodium ion batteries.



Yufeng Zhao is currently working as a professor at Shanghai University. She obtained her PhD from Nanyang Technological University, Singapore in 2006. Afterward, she worked at Deakin University, Australia (2006–2008) and Phillips University Marburg, Germany (2008–2009) as a research scientist. She was also a visiting professor at the Northwestern University (2014–2015). Her research mainly focuses on energy-storage materials and devices, such as nanocarbon materials, supercapacitors, and electrocatalysts.



Juan Wang is currently working as a professor at Xi'an University of Architecture and Technology. She obtained her PhD from Xi'an University of Architecture and Technology in 2009. Afterward, she worked as a visiting research fellow at Georgia Institute of Technology (2013–2014). Her research interests focus on energy storage materials for power sources, including Li–S battery and Li/Na-ion battery.



Yanglong Hou earned his PhD in materials science from Harbin Institute of Technology in 2000. After a short postdoctoral training at Peking University, he worked at the University of Tokyo (2002–2005) as a JSPS foreign special researcher and also at Brown University (2005–2007) as a postdoctoral researcher. He joined Peking University in 2007. His research interests include the design and chemical synthesis of functional nanoparticles, and their biomedical and energy-related applications.

耐久的P2型层状氧化物正极材料的低温储钠性能研究

李勇^{1,2}, 赵玉峰^{1,2*}, 冯晓晨^{2,3}, 王轩², 石钦昊², 王静³, 王娟^{1*}, 张久俊², 侯仰龙^{4*}

摘要 为实现大规模储能, 钠离子电池不仅需要高的能量密度, 而且需要在低温环境下依旧发挥出良好的性能。拥有高比容量的P2锰基氧化物被认为是钠离子电池中理想的候选正极材料, 但是其低温应用却很少被探索。本文通过合理的结构调整, 制备了具有优异低温性能的P2型 $\text{Na}_{0.67}\text{Ni}_{0.1}\text{Co}_{0.1}\text{Mn}_{0.8}\text{O}_2$ 正极材料。该材料表现出了优异的钠离子扩散系数 ($\sim 10^{-9} - 10^{-7.5} \text{ cm}^2 \text{ s}^{-1}$, -20°C)。在半电池体系中, 该材料拥有 $147.4 \text{ mA h g}^{-1}$ 的低温放电容量。同样在 -20°C 条件下, 该电极材料也展现出能量密度为 $358.3 \text{ W h kg}^{-1}$ 的出色的全电池性能。各种表征和密度泛函理论计算表明固溶反应和赝电容特征促进了钠离子从电极体相到界面的扩散和脱溶剂化过程, 最终在低温条件下能够获得优异的电化学性能。